Controlling $CaCO_3$ particle size with $\{Ca^{2+}\}:\{CO_3^{2-}\}$ ratios in aqueous environments

Sergĕj Y. M. H. Seepma*,[a] Sergio E. Ruiz-Hernandez,[a] Gernot Nehrke,[b] Karline Soetaert,[ac] Albert P. Philipse,[d] Bonny W. M. Kuipers,[d] Mariette Wolthers[a]

[a] Utrecht University, Department of Earth Sciences, Princetonlaan 8A, 3584 CB Utrecht, The Netherlands

[b] Alfred-Wegener Institut: Helmholtz-Zentrum für Polar- und Meeresforschung, am Handelshafen 12, 27570 Bremerhaven, Germany

[c] NIOZ: Royal Netherlands Institute for Sea Research, Estuarine & Delta Systems Department, Korringaweg 7, 4401 NT Yerseke, The Netherlands

[d] Utrecht University, Van 't Hoff Laboratory for Physical and Colloid Chemistry, Debye Institute for Nanomaterials Science, Padualaan 8, 3584 CH Utrecht, The Netherlands

---

Supporting Information

SI --- Experimental Set-Up

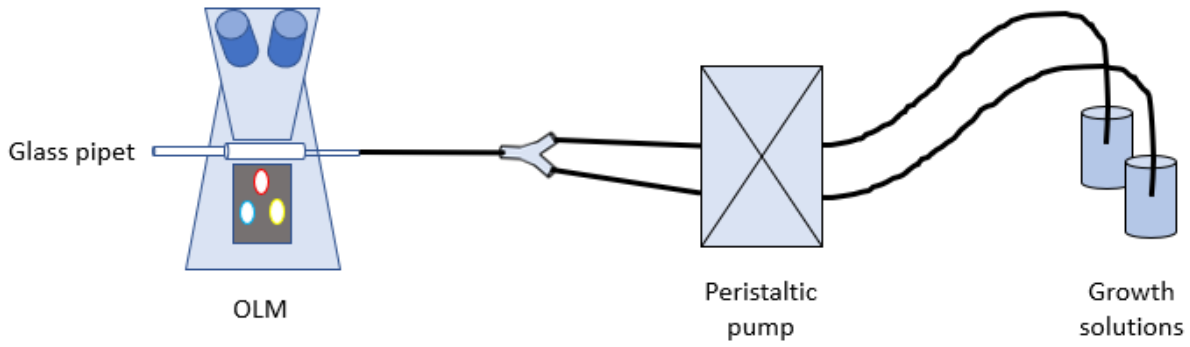

Figure S1: XPL's Experimental set-up.

SII --- Physical and optical behavior of $CaCO_3$ under XPL

$CaCO_3$ crystals appear as bright, white and flickering dots in XPL, due to the fact that vaterite, aragonite and calcite are anisotropic and cause birefringence.[1,2] Nevertheless, the optical effect of birefringence during and after $CaCO_3$ nucleation, until it settles on the inner wall, is caused by constant tumbling of $CaCO_3$ crystals within a tube, rather than a rotating stage of the microscope during XPL experiments. At some point after their settling, the crystals do not illuminate anymore and, as some longer time passes, start to disappear again. The explanation for this phenomenon lies in the relationship between the transmitted light intensity of two distinct propagated light waves[3]:

$$I = A^2 \sin^2(2\varphi) \sin^2\left(\frac{\pi d}{\lambda}(\mu_E - \mu_O)\right) \qquad \text{(S2.1)}$$

where 'A' is the amplitude of the light [W m^{-2}], 'φ' the angle [°] between the resultant vibration direction that is allowed with respect to the orientation of the polarizer, 'd' the thickness of the crystal [m], 'λ' the wavelength of

the absorbed light [m] and 'μ_E' and 'μ_O' the refractive indices [-] of, respectively, the E-ray and O-ray. If $\varphi = 90°$, then the situation, called the extinction position, occurs, meaning that the intensity of transmitted light is zero. Contrary, when $\varphi = 45°$, the first sinusoidal-term in Equation S2.1 becomes unity. Therefore, at this angle, the crystal is illuminated to its fullest.

The second sinusoidal term contributes also to the light intensity and is mainly dependent on the crystal thickness (d).[2] Comparing the contribution of this term using different crystal sizes explains the phenomenon why crystals undergo the stages of flickering, brightly present and disappearance during growth (Figure S2).

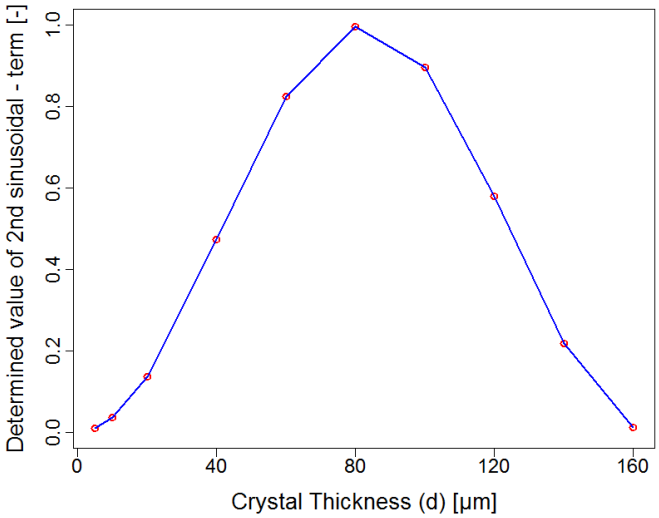

Figure S2: Graph illustrating the relationship between the crystal size and the contribution of the 2nd sinusoidal term to light intensity (with λ=500 and using the refractive indices for calcite; 1.658 and 1.485).

SIII --- Definition of precipitation time

Whenever two crystals visibly settled on the wall of the tube, then this time was recorded, and was defined as the precipitation time accordingly (Figure S3).

Based on the relationship depicted in Figure S2, we derived that crystals visible in XPL are at least 20 μm thick in the direction of the polarized light beam. Note however, that this curve holds for $\varphi = 45°$. If crystals happened to form at or near the extinction angle, we did not observe them, since we did not rotate the setup relative to the light source.

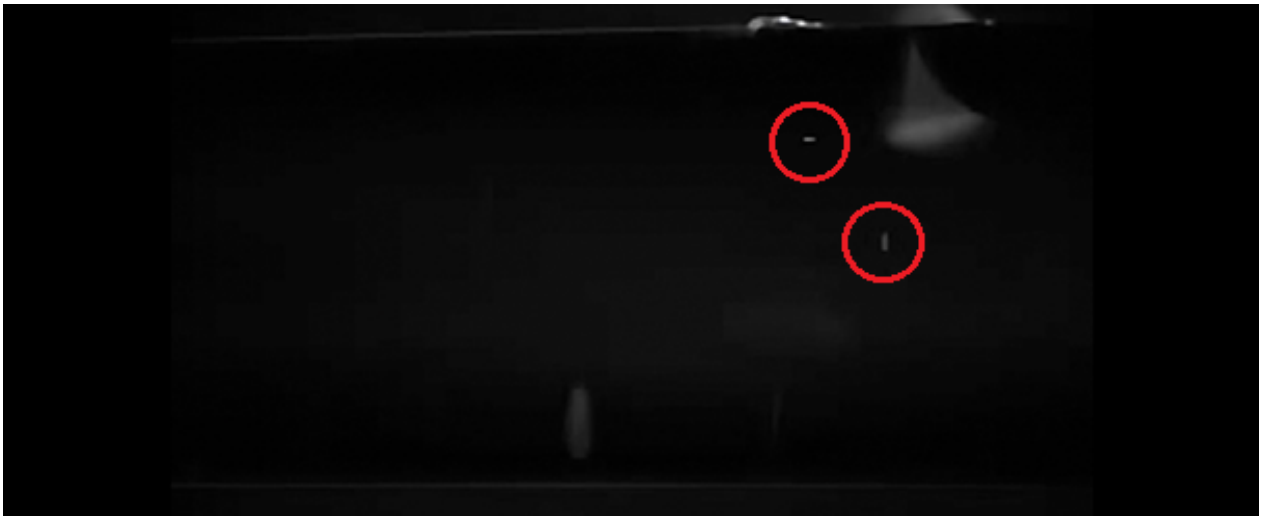

Figure S3: The moment at which the precipitation time is defined. Two crystals are visible: the one located slightly at the top wall of the tube is visually sharp and was therefore settled on the upper part of the wall. The one located in the middle of the tube is observed more vaguely under XPL and was, consequently, settled on either the top or bottom wall (since the focus was not on either of these wall parts).

SIV --- Derivation of the proposed fitting equation

The initial method that used to create the model, which describes the precipitation time of $CaCO_3$ with respect to ionic strength, pH, supersaturation degree and stoichiometry between Ca^{2+} and CO_3^{2-}, is the 'Non-linear least squares (nls)'. Subsequently, the initial equation was refined and simplified using a Bayesian approach (Section V). The greatest advantage of using nls regression over many other technique is the broad range of functions that can be fitted. One other advantage is the efficient use of data. Nonlinear regression can produce good estimates

of the unknown parameters in the model with relatively small data sets.[4] The disadvantage is that this technique requires starting values or initial guesses of the still unknown parameters. To have an initial starting value for the unknown parameters, trial and error guesses were carried out to approximate the model function to an arbitrary line along the measured data points, where the relationship of Ω, pH and *I* with nucleation time were deduced from earlier work of Nielsen (1964),[5] Wolthers et al. (2012)[6] and Zuddas & Mucci (1998),[7] respectively, which is described below.

The nls-method was performed within R-software environment.[8] The algorithm used to converge the model is the 'nl2sol' (named 'port' within R Studio). This algorithm minimized the nonlinear sum of squares using an analytical Jacobian, which is used in reaction kinetics quite often.[9-11] It assumes that there is a certain amount of variables 'X' and an equivalent number of nonlinear "residual functions" 'F(X)' and the algorithms' task is to find a solution 'X' that minimizes the Euclidean norm of '| | F(X) | |'.[12] Bates & Watts (1988)[13] and Chambers (1992)[14] provide more information about the used algorithm and associated mathematics behind it.

The non-linear model that was implemented to fit the measured data was based on four dependent and 8 independent (fitting) parameters:

$$Nucleation\,time\left(r_{aq},\Omega_{cal},pH,I,i,j,k,l,m,n,o,p\right) =$$

$$\left(\left(\frac{r_{aq}^{i}+j}{r_{aq}*k}+r_{aq}^{l}+m\right)*\left(\left(\sqrt{\Omega_{cal}}\right)-1\right)^{n}*\left(pH^{o}\right)*\left(\frac{1}{I}\right)\right)*p \qquad \text{(S4.1)}$$

where "p" consists of several parameter constants ("p1, p2...") (Table S4.1).

NOTE: *For clarity, the letters indicating the fitting parameters are denoted by different letters compared to Equation 4, as they have different values due to the fact that Equation S4.1 is written in the initial different form.*

Table S4.1: Parameter values used in the 'nls'-model.

Parameter	Model Value
m [-]	*300
n [-]	-7.0
o [-]	-10.99
p [M sec]	$2.3 * 10^9 * 0.148 * 4.5625 * 10^9$

* Except at Ω = 50, where 'm' = 0

Evaluation of the supersaturation (Ω) term

Different rate laws for $CaCO_3$ crystal growth regarding supersaturation have been proposed in the past. One that is often used to fit experimental data relates crystal growth to supersaturation[5,15,16] and this relationship is assumed for $CaCO_3$ precipitation as well:

$$J_g = k * (\Omega_{cal} - 1)^n \qquad \text{(S4.2)}$$

where 'J_g' is the precipitation rate [$m^3\ s^{-1}$], 'k' is the rate constant [$m^3\ s^{-1}$] and 'n' is an empirical reaction order [-]. Basically, the $CaCO_3$ precipitation rate increases as the supersaturation of $CaCO_3$ in the solution increases. A similar relation to link Ω_{cal} to precipitation time has been used in this research. For the results of this study, Ω_{cal} related to precipitation time through the square root of Ω_{cal}, especially if $10 < \Omega_{cal} < 50$ (Figure S4.1). Therefore, the following dependency was applied:

$$precipitation\,time = p1 * (\sqrt{\Omega_{cal}} - 1)^n \qquad \text{(S4.3)}$$

where 'p1', in Equation S4.3, has a fitted value of $2.3*10^9$ [sec] and n = -7.0 delineated by the blue fit in Figure S4.1. Equation S4.2 would be better applicable if $\Omega_{cal} \geq 150$. Potentially, this is due to a switch in the precipitation mechanism above $\Omega_{cal} > 100$ from nucleation and growth to nucleation and aggregation (and

transformation). Accordingly, parameter 'p1' in Equation S4.3 was adjusted by one order in magnitude, to a value of $2.3*10^{10}$ at $\Omega_{cal} = 200$, resulting in a better fit.

NOTE: *one extra precipitation time measurement was conducted at* $\Omega_{cal} = 30$ *in order to find an indication of the relationship between* Ω *and precipitation time, as plotted in Figure S4.1.*

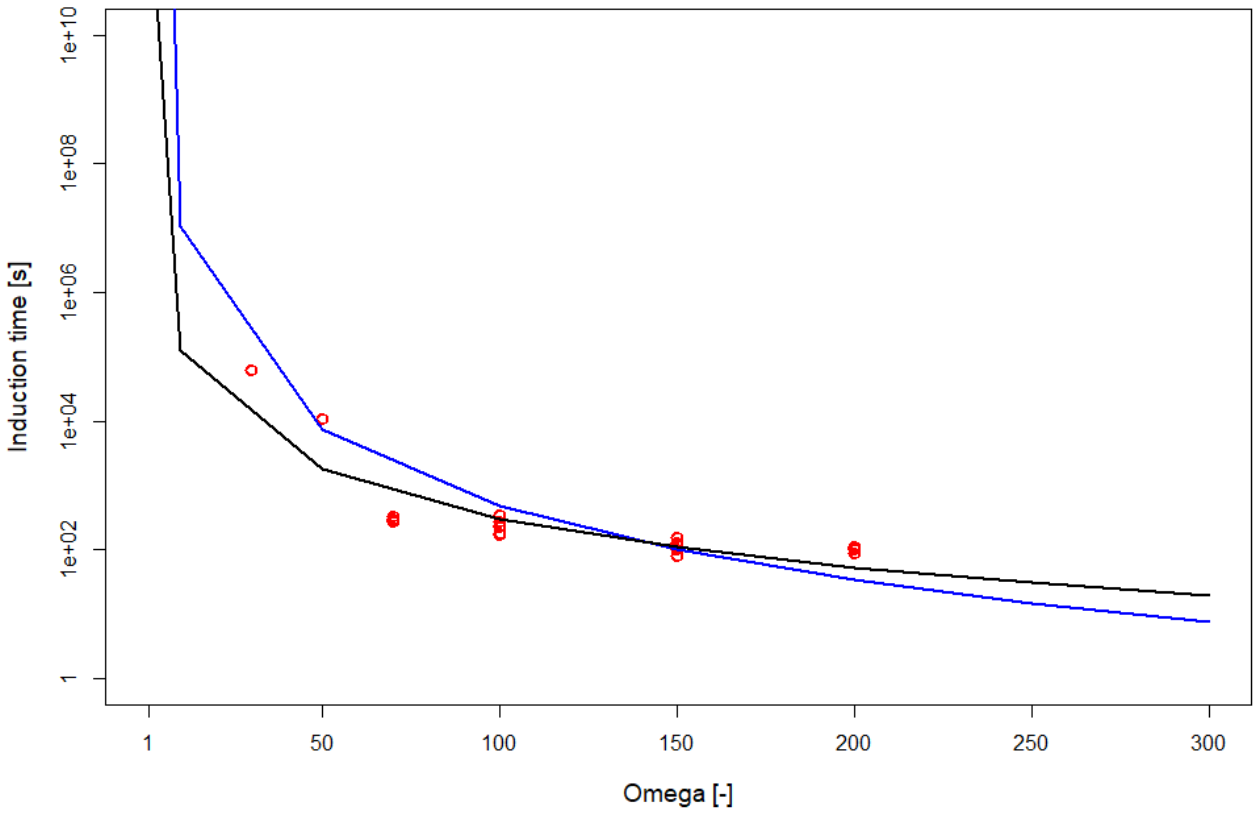

Figure S4.1: Relation between Ω and precipitation time shown based on conducted experiments in this research. One extra measurement has been done at Ω = 30, stoichiometry ~ 1, pH ~ 11 and *I* ~ 0.19-0.20 M. The blue curve represents the dependency between Ω and precipitation time as stated in Equation S4.3, whereas the black fit represents an exponential dependency without any square root as can be delineated from Equation S4.2. The former one seems to have a better fit whenever Ω < 150. The better fit is further supported by a smaller value of least squares.

Evaluation of the pH term

It is commonly believed that the effect of pH on $CaCO_3$ precipitation time is similar to the pH impact on crystal growth.[17] Wolthers et al. (2012)[6] pointed out that there is an exponential relationship between pH and growth of individual $CaCO_3$ crystals. The exponent they used to model the calcite growth rate was -10.99. Considering the

fact that the pH mainly effects the solubility of $CaCO_3$, our precipitation time must have a similar trend with pH as shown in Figure S4.2. The value of -10.99 was therefore adopted in the exponent to investigate the relation between pH and precipitation time (Figure S4.2). Concluding from Figure S4.2, the $CaCO_3$ precipitation happens roughly a hundred times faster at pH 11 than at pH 7.5. A similar relation was also found by Gómez-Morales et al. (1996).[18]

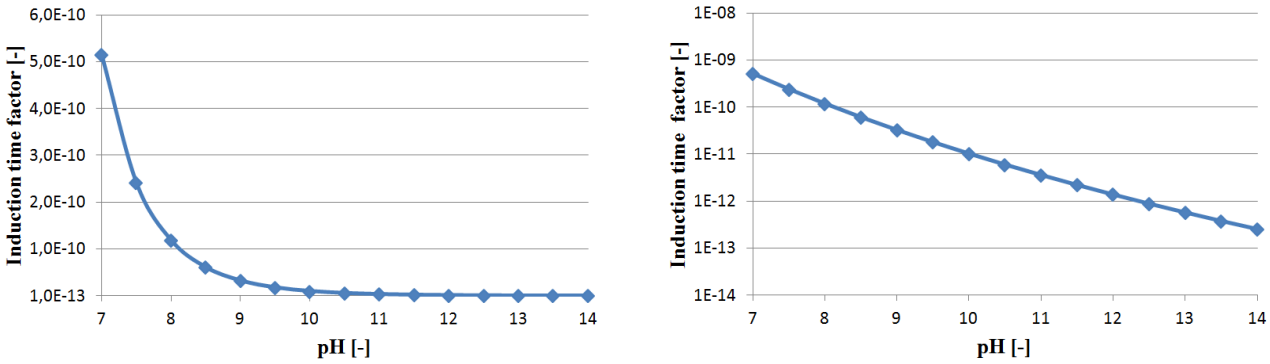

Figure S4.2: The effect that pH has on the precipitation time on a linear scale (left) and a logarithmic scale (right).

Evaluation of the Ionic Strength term

Zuddas & Mucci (1998)[7] investigated the relationship between ionic strength and precipitation rate. The results obtained in their study reveal that the partial reaction order with respect to the carbonate ion concentration increases linearly as a function of total ionic strength. A one- to four-fold increase in the partial reaction order is expected upon a ten-fold increase in ionic strength.

However, this relationship is very specific for NaCl as the background electrolyte and this linear expression is only valid if ~ $0.05 < I < 1.0$ M. Beyond this range, the activity for NaCl does not behave linear anymore with increasing or decreasing ionic strength.[19] Since we worked at 0.2M NaCl, the relationship found by Zuddas & Mucci (1998)[7] was used here to represent the effect of ionic strength on precipitation time obtained in XPL precipitation experiments. Conversion factors, to correct our measurement times for minor variations in ionic strength in our experiments, are found in Table S4.2. These conversion factors were based on the slope of the

line in Figure 6 in the study of Zuddas & Mucci (1998)[7], which relates the kinetic impact of ionic strength variations, and has a slope of 3.7.

Table S4.2: Used conversion factor to correct for differences in ionic strength among the different solutions.

Solution nr.	Calculated conversion factor
2.1	2.79
3.1	3.19
4.1	3.51
5.1	4.58
5.6	1.21
5.7	*6.23
6.1	1.14
6.5	1.54

*Slightly outside linear part according to Garrels & Christ (1965).

Yet, the figure relates ionic strength to a rate rather than a time. If a rate is positively correlated to ionic strength then the precipitation time is inversely related to ionic strength. This inverse relation exists because, for example, a higher chance of collision between two ions translates to a faster nucleation process, leading to a decline of induction time and ultimately affects our measured precipitation time. Therefore, the term in Equation S4.1. that includes ionic strength, is characterized by an inverse relation, where the associated parameter 'i' is assumed to have a value of 6.757 M^{-1} and the inverse number (0.148 M) can be found as a part (‘p2’) of parameter 'p' in the final equation (Equation S4.1) in order to account for differences in ionic strength at extreme stoichiometric conditions. The derivation of the constant value of ‘i’ was obtained via (where 0.7M was used as an example, but any other value of *I* would lead to the same result):

$$\frac{0.7}{0.2}=3.5$$

$$\frac{1}{0.2i}-\frac{1}{0.7i}+\frac{(0.2*3.7)}{3.5}-(0.2*3.7)\ =\ 0, \text{ so}$$

$$i=6.757[M^{-1}]$$

Ultimately, parameter “i”, “j”, “k” and “l” of Equation S4.1 were computed in order to fit the measured data as all other fitting parameters were assigned with a constant value based on past research described above (Table S4.1). ‘p3’ = $4.5625*10^{-9}$ was introduced as an empirical value (factor) to complete the fitting with p = p1 * p2 * p3.

nls results

Using the nls method, parameter values were obtained for “i”, “j”, “k” and “l” (Equation S4.1) for each dataset (Ω) (Table S4.3); the fit of the initial equation to the experimental data is shown in Figure S4.3.

Table S4.3: Parameter values obtained by nls-fitting of Equation S4.1.

Ω	i	j	k	l	m
200	0.607	0	0.0265	0.670	300
150	1.230	0.0126	0.0009	0.991	300
100	1.029	0.00118	0.000183	1.261	300
85	0.943	0.00139	0.00381	1.566	300
70	2.562	0.818	1.184	1.612	300
50*	2.562	0.610	0.902	1.80	0

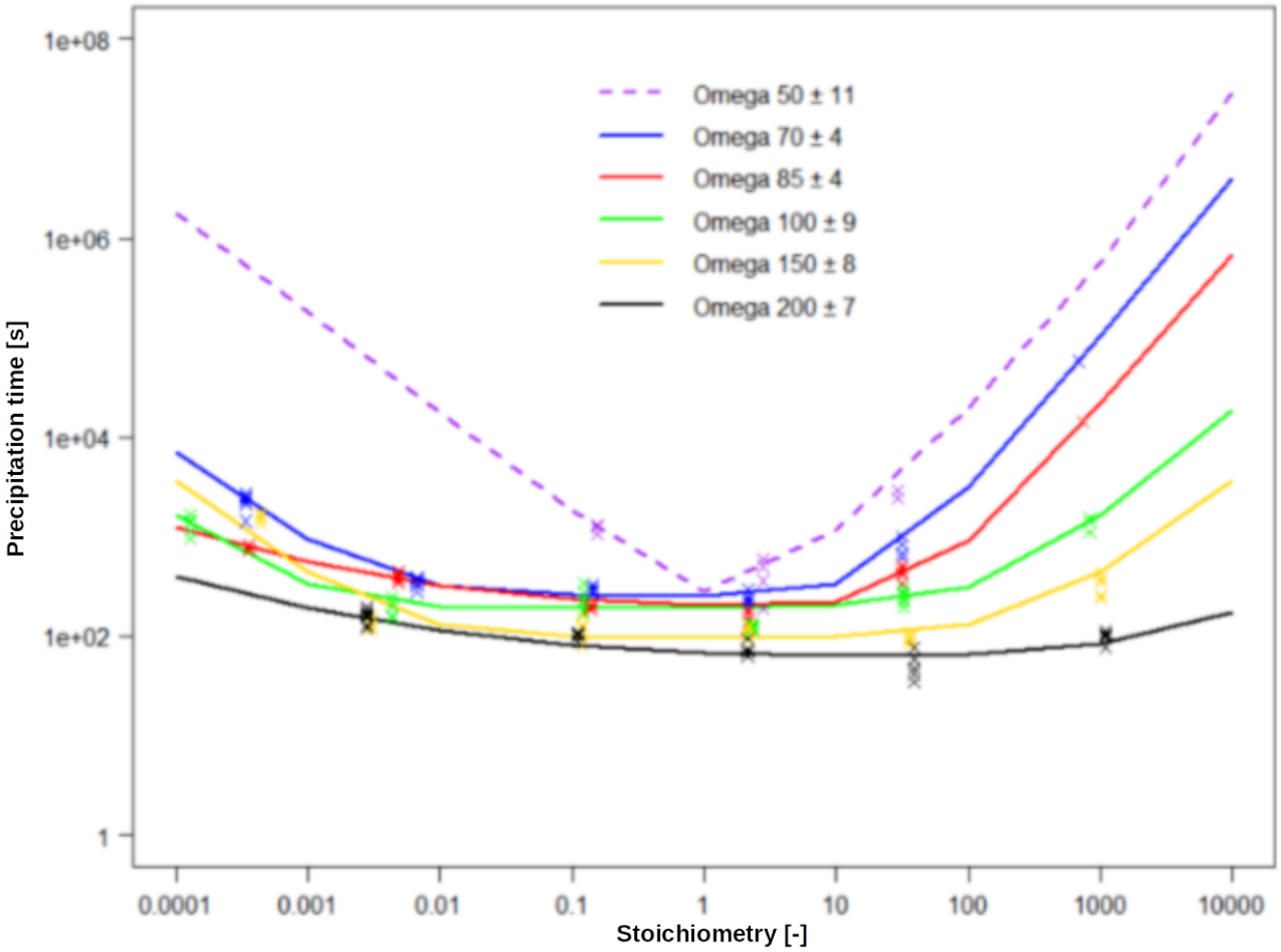

Fig S4.3: The relationship between induction time and stoichiometry at different supersaturation degrees. Crosses are precipitation times measured using XPL-OLM; lines are initial fits, obtained with the nls method. Final fits to this data set, obtained after a refinement using a Bayesian approach, are shown in Figure 5 in the main text.

However, Equation S4.1 and Table S4.3 show that there was a potential co-linearity between "j" and "k". This was further investigated using a Bayesian approach in order to simplify the proposed underlying modelling equation (Equation S4.1). Additionally, the 'nls'-approach did not allow us to calculate the confidence interval for the overall equation and was solved by using the Bayesian approach.

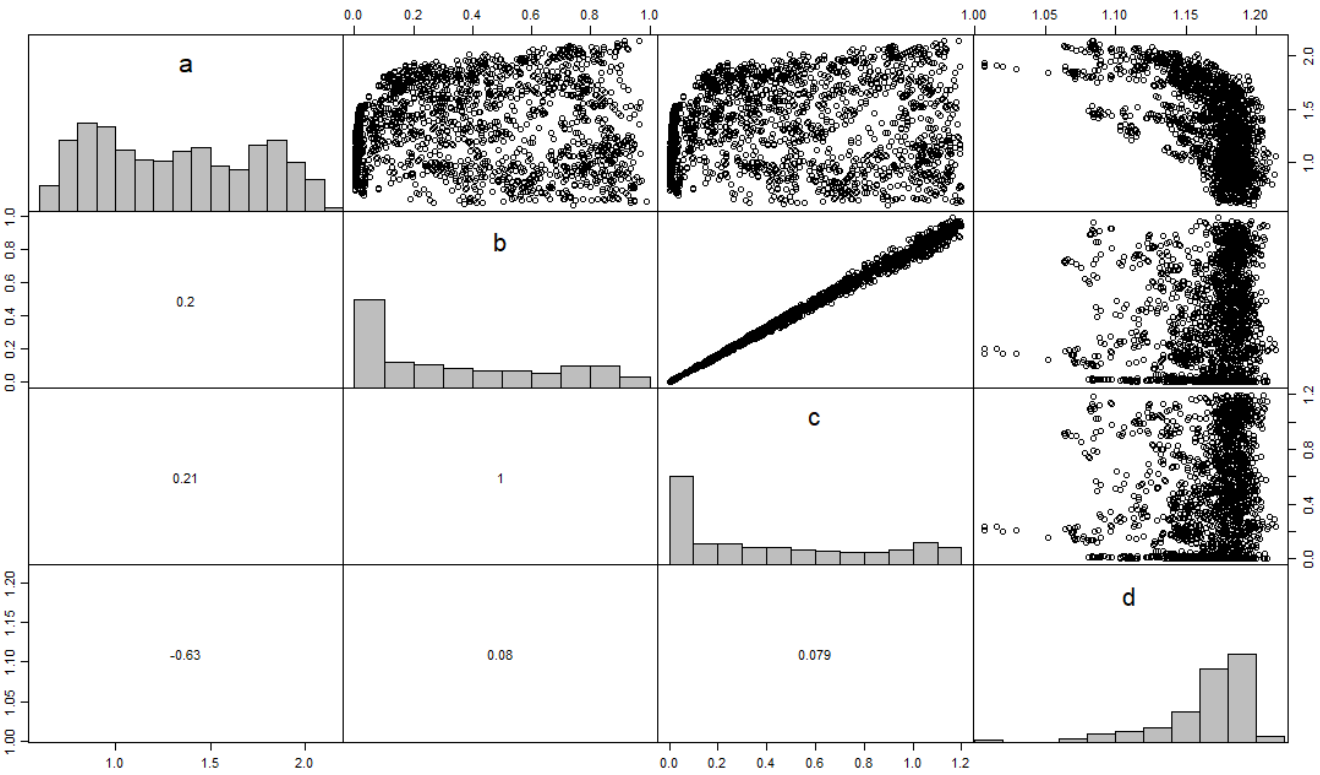

Figure S4.4: Matrix correlation plot corresponding to Equation S4.1 and the dataset with Ω = 100.

SV --- Bayesian Statistics

The initial proposed equation obtained by nls (Equation S4.1) was simplified (Equation S4.4) by applying Bayesian statistics in order to reduce the amount of fitting parameters. The Bayesian modelling approach allows for evaluation of the parameter sensitivities for those that relate the stoichiometry to precipitation time. For clarity, we relabelled the various parameters from Equation S4.1. The co-linearity between "b" and "c" (previously "j" and "k") was clearly revealed as is depicted in the matrix correlation plot (Figure S4.4). According to Figure S4.4, the correlation between parameter "b" and "c" is 1, which means that they show a very strong colinearity. Therefore, the proposed equation (Equation S4.1) was rewritten in such a way that there is no colinearity between these two parameters; [c = 1.2b]. Also, "m" was removed from Equation S4.1 in the process, as the improvement of fitting was very little, resulting in a more simplified equation for the precipitation time (see also Equation 4 in main text):

$$t_{nucleation}\left(r_{aq}, \Omega_{cal}, pH, IS, a, b, c, d, e, f\right) = \left(\left(\frac{r_{aq}^{a}+b}{r_{aq}*1.2\,b}+r_{aq}^{c}\right)*\left(\left(\sqrt{\Omega_{cal}}\right)-1\right)^{d}*\left(pH^{e}\right)*\left(\frac{1}{IS}\right)\right)*f \quad \text{(S4.4)}$$

NOTE: In Equation S4.4, the fitting parameters are assigned by different letters, as they have different values compared to Equation S4.1.

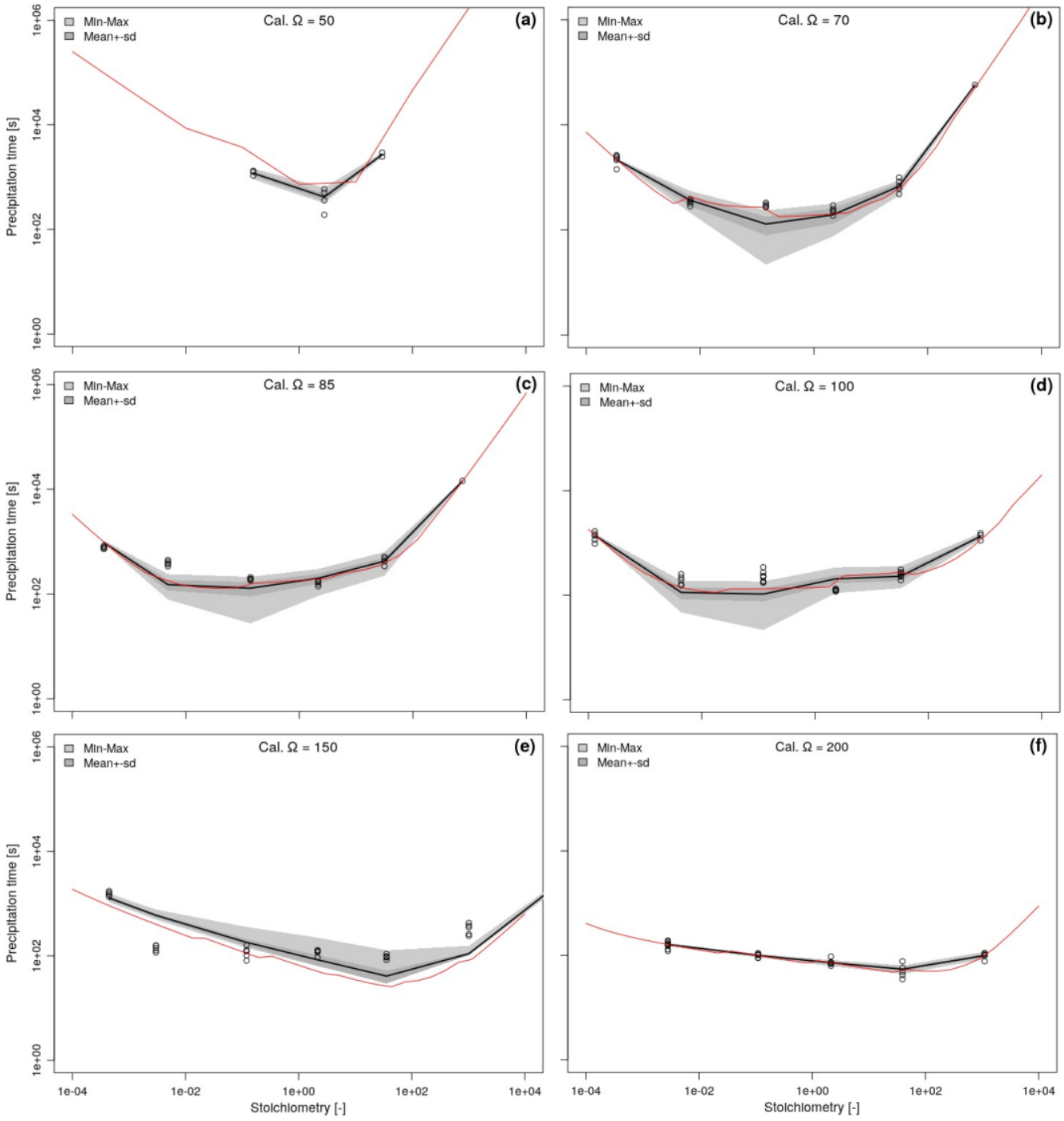

Figure S5: Predictive inference plots for each omega dataset. The red line gives the best fit, while the black line shows the average of 3000 randomly chosen MCMC computations; the dark grey envelopes indicate the ± 1 standard deviation and the light grey the min-max probability fields.

Table S5: Statistics output for each dataset of omega-value.

Omega = 200			
Parameter	Estimate	Std. Error	P-value
a	0.827	0.0101	e^{-16}
b	$2.28e^{-4}$	$1.16e^{-5}$	e^{-16}
c	1.13	$1.58e^{-2}$	e^{-16}

Omega = 85			
Parameter	Estimate	Std. Error	P-value
a	1.074	0.0516	e^{-16}
b	0.00233	0.00039	$3.6e^{-6}$
c	1.5005	0.00213	e^{-16}

Omega = 150			
Parameter	Estimate	Std. Error	P-value
a	0.600	0.1482	0.0003
b	0.001	0.00109	0.366
c	0.981	0.00573	e^{-16}

Omega = 70			
Parameter	Estimate	Std. Error	P-value
a	1.052	0.0548	e^{-16}
b	0.00477	0.00095	$3.5e^{-5}$
c	1.585	0.00079	e^{-16}

Omega = 100			
Parameter	Estimate	Std. Error	P-value
a	1.034	0.0507	e^{-16}
b	0.0016	0.00026	$1.3e^{-6}$
c	1.167	0.0179	e^{-16}

Omega = 50			
Parameter	Estimate	Std. Error	P-value
a	0.2933	0.1064	0.033
b	0.0115	0.0022	0.002
c	1.8353	0.0159	$2.9e^{-11}$

The initially allowable lower and upper boundaries for the unknown fitting parameters “a”, “b” and “c” in the Bayesian approach were set at 0.6, 10^{-3}, 0.6 and 2.6, 1.0 and 1.8, respectively. Table S5 and Figure S5 show the final results from the parameter evaluation.

In most cases, the measured precipitation times related well to the precipitation times calculated using Equation S4.4. At $\Omega = 50$, the estimates and associated standard errors show slightly higher p-values, but are still well below the accepted cutoff ($P < 0.05$). Also, the parameter estimates and associated standard errors are a bit less accurate compared to the ones computed for larger Ω-values, as the dataset of $\Omega = 50$ contains fewer measurements. However, the “b” parameter at $\Omega = 150$ shows a large p-value, because the Ca-limiting solutions ($r_{aq} < 1$) do not show a significant increase in precipitation time as was the case at other Ω-values, making it the only result that implies weak evidence against the null-hypothesis (e.g. relationship between measurements and fit).

Generally, as depicted from Table S5, the “b” and “c” parameter value increased with decreasing Ω, while the “a” parameter does not show any definite response to Ω. Figure S5 reveals that some measurements fall outside

the minimum-maximum probability fields. Causative might be the measurement error that has not been incorporated in the model.

SVI --- Three-hour time range of the $CaCO_3$ particle size evolution (both intensity and number vs. size plots) at r_{aq} = 1

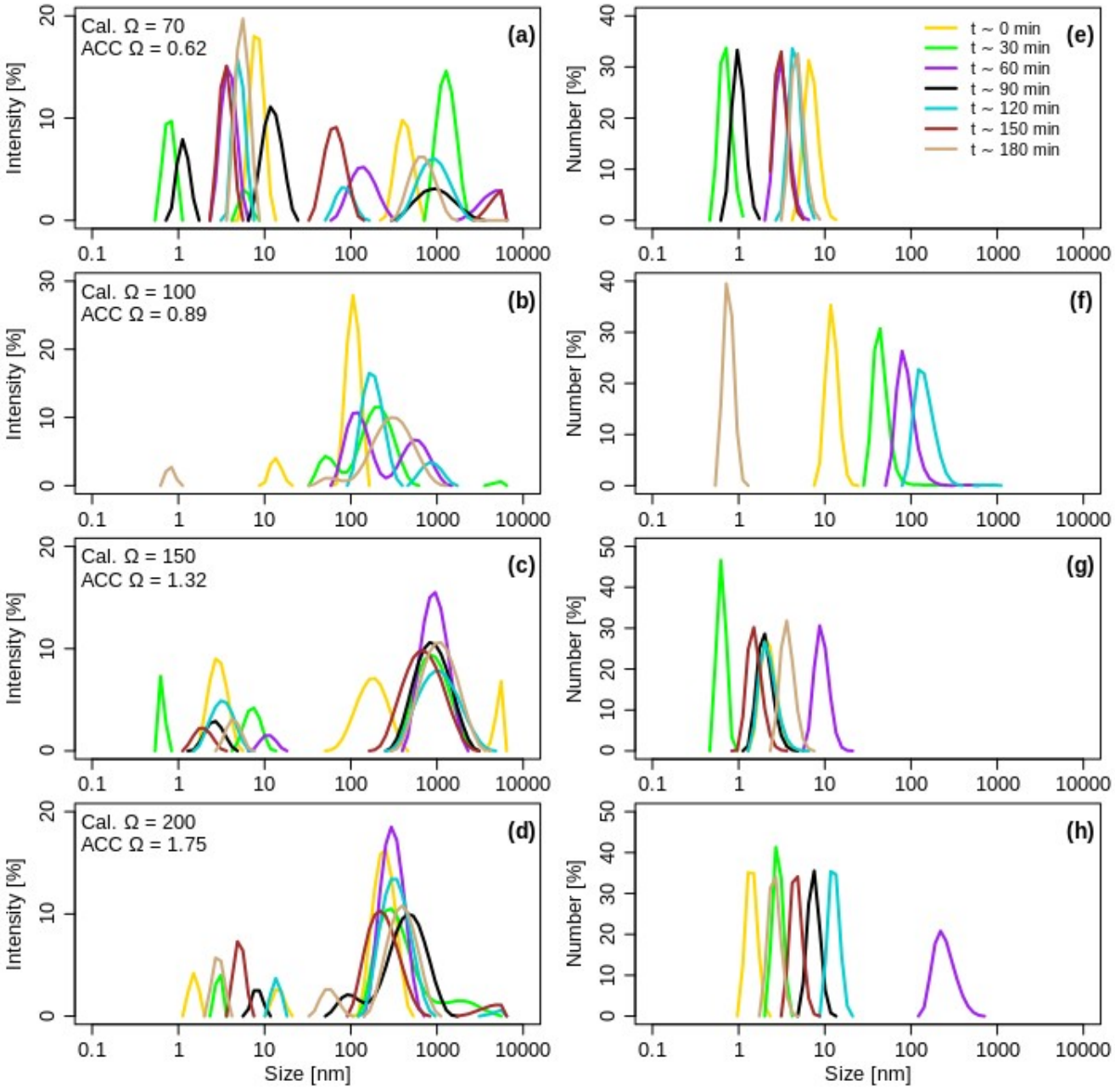

Figure S6: The relative intensity of scattered light [%] vs particle size [nm] (a-d) and the relative amount of particles (number) plotted against the size of particles [nm] (e-h), at stoichiometric conditions at different Ω_{cal} (i.e. 70, 100, 150 and 200) for the first three hours of the precipitation reaction. Note that for Ω_{cal} = 100, only five measurements were performed (instead of seven).

SVII --- The 15-hour time range of the $CaCO_3$ particle size evolution (number vs. size plots) at r_{aq} = 1 at different Ω

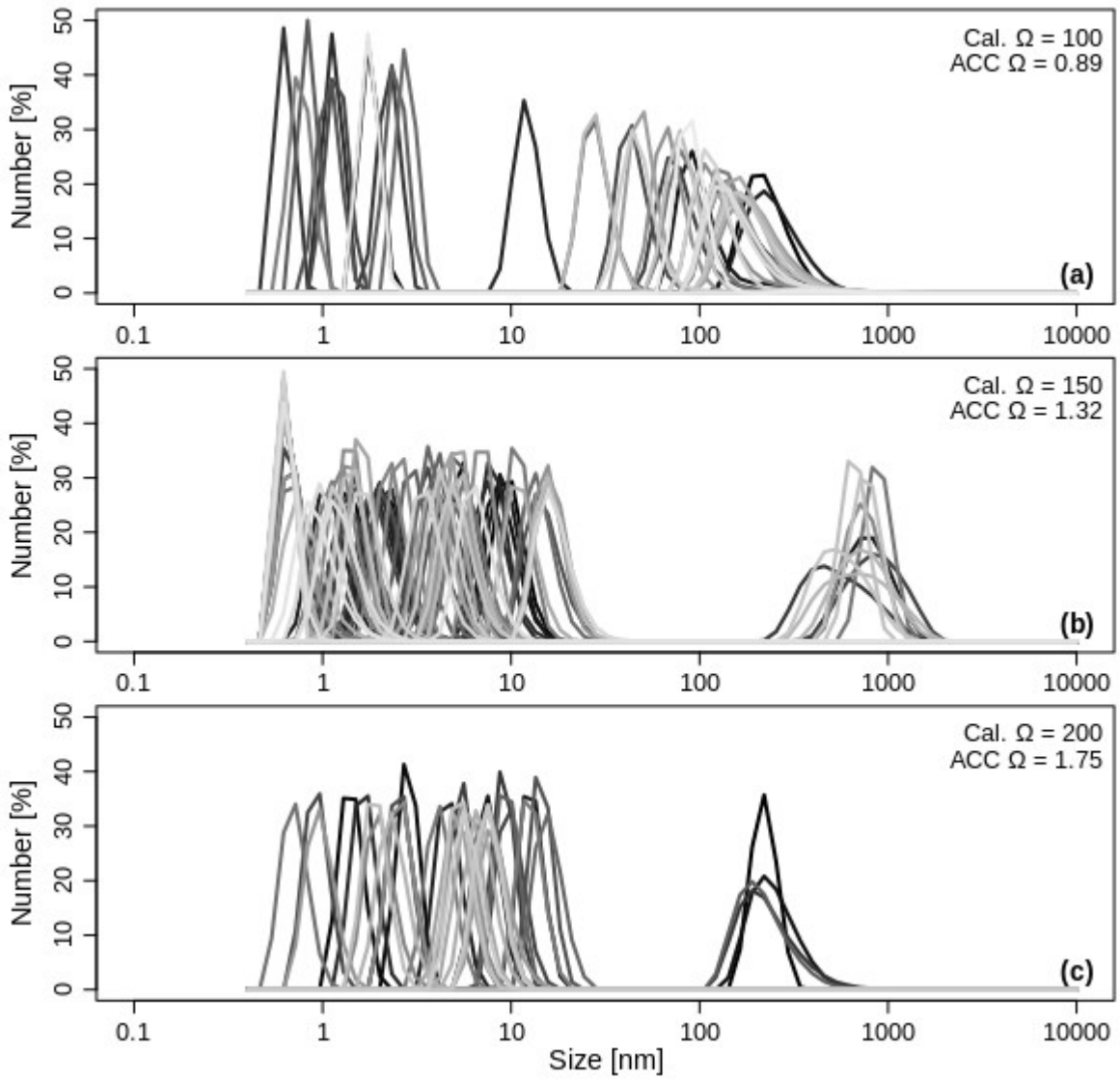

Figure S7: Measurements were taken for 15 consecutive hours. The upper and bottom figure consist of measurements taken roughly every 30 minutes, while the time interval for the middle one was set at roughly 10 minutes. The darkest gray-scale color represents the first time step and subsequential time steps become more and more brighter. The preference between both nucleation and growth pathways may play a role as small precipitate-sized particles (30 – 100 nm) were not seen at Ω > 100 and their absence may indicate that nucleation and growth occur by aggregation of prenucleation clusters.

SVIII --- one-hour time range of the $CaCO_3$ particle size evolution (both relative intensity and number vs. size plots) at $r_{aq} \neq 1$

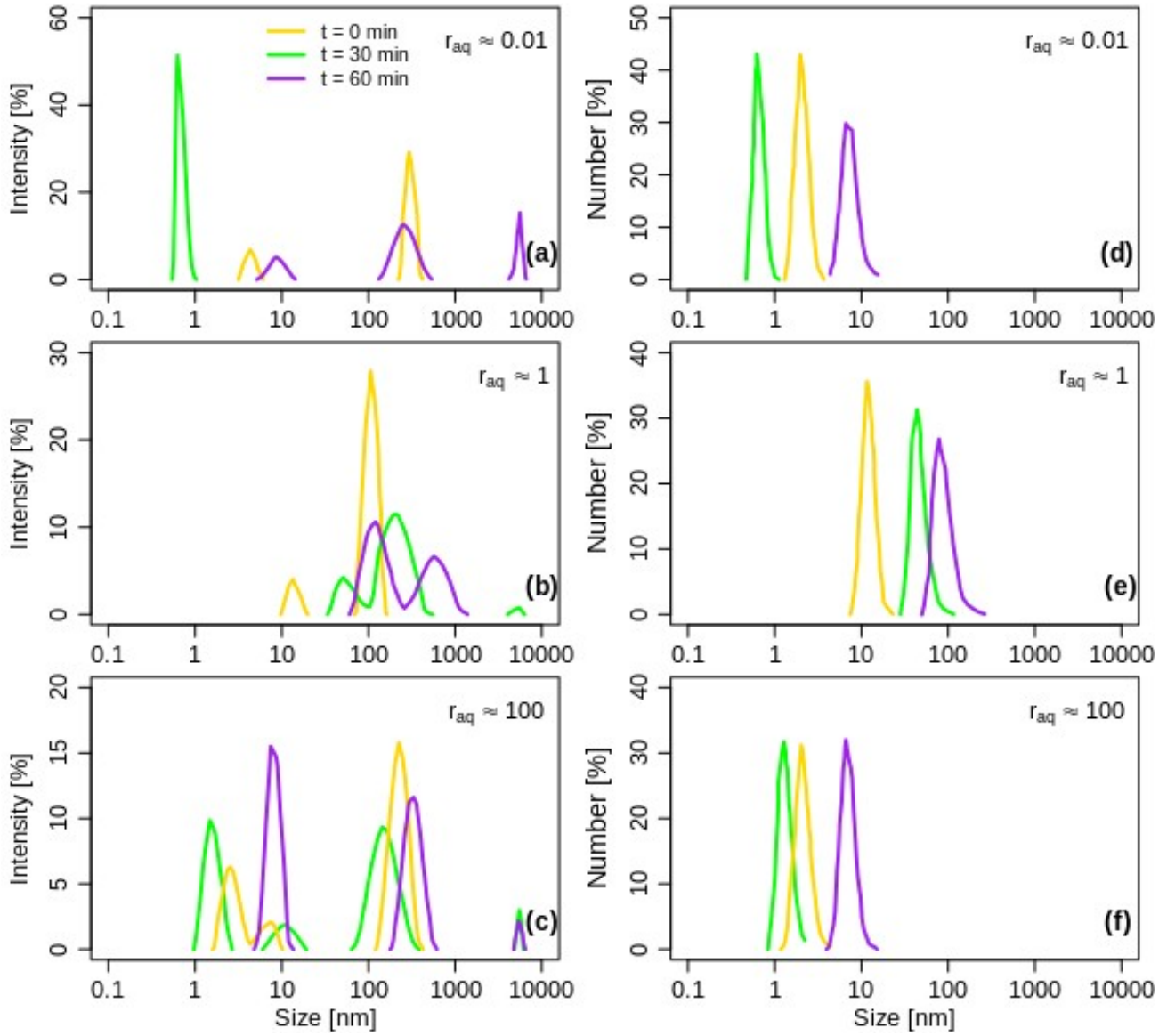

Figure S8: The relative intensity of scattered light [%] vs particle size [nm] (a-c) and the relative amount of particles (number) plotted against the size of particles [nm] (d-f), at different stoichiometric conditions at an Ω_{cal} = 100 for the first hour of the precipitation reaction. In all cases, the yellow color represents a rough initial measurement, the green colour after approximately half an hour and the purple colour represents a measurement after one hour.

SIX --- Three-hour time range of the $CaCO_3$ particle size evolution with time (both relative intensity and number vs. size plots) at $r_{aq} \neq 1$

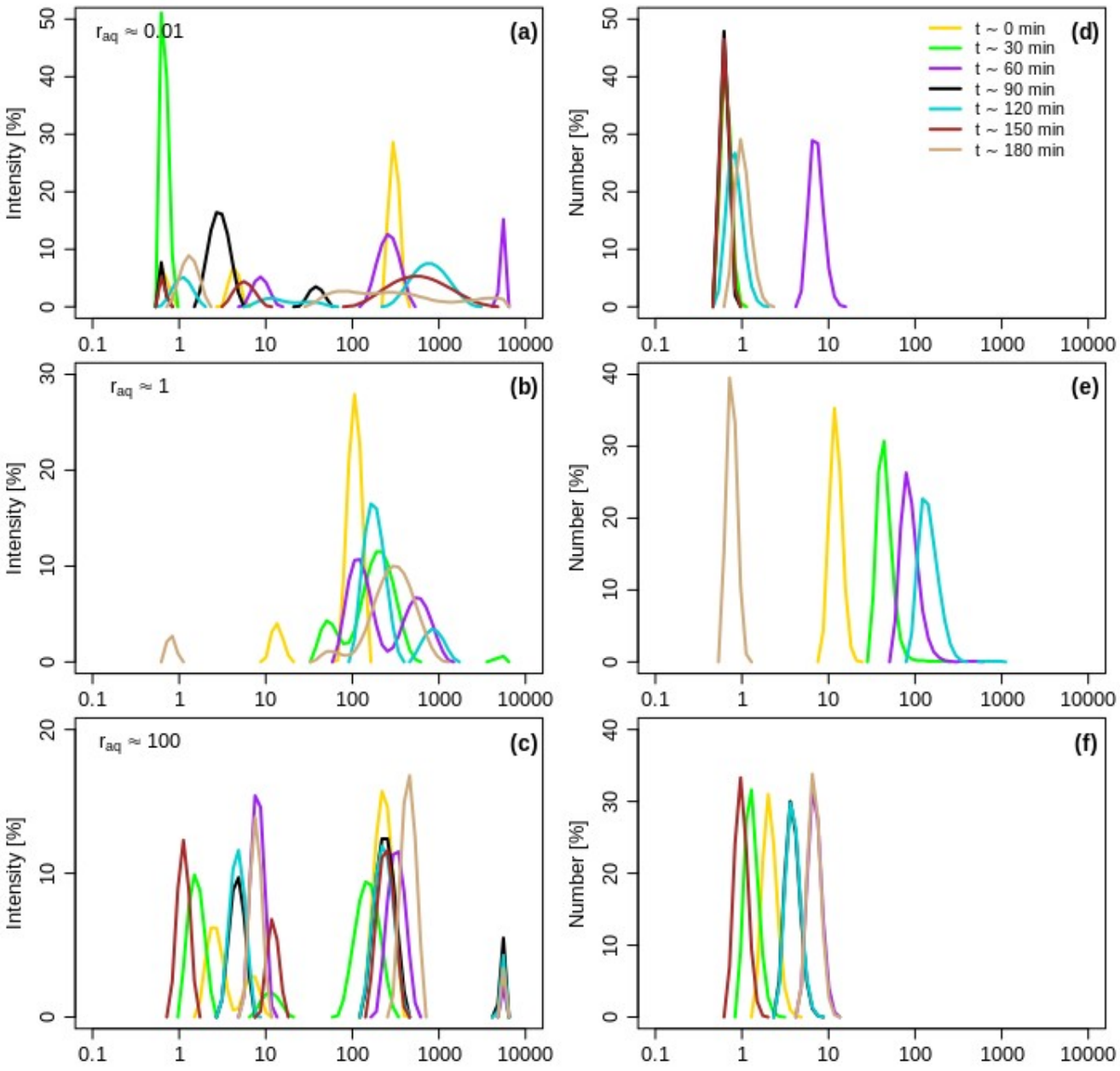

Figure S9: The relative intensity of scattered light [%] vs particle size [nm] (a-c) and the relative amount of particles (number) plotted against the size of particles [nm] (d-f), at different stoichiometric conditions at an Ω_{cal} = 100 for the first three hours of the precipitation reaction. Note that for Ω_{cal} = 100 at $r_{aq} \approx 1$, only five measurements were performed (instead of seven). Also, some peaks may overlap.

SX --- Thermodynamic stability over time for the systems we used in our MD simulations

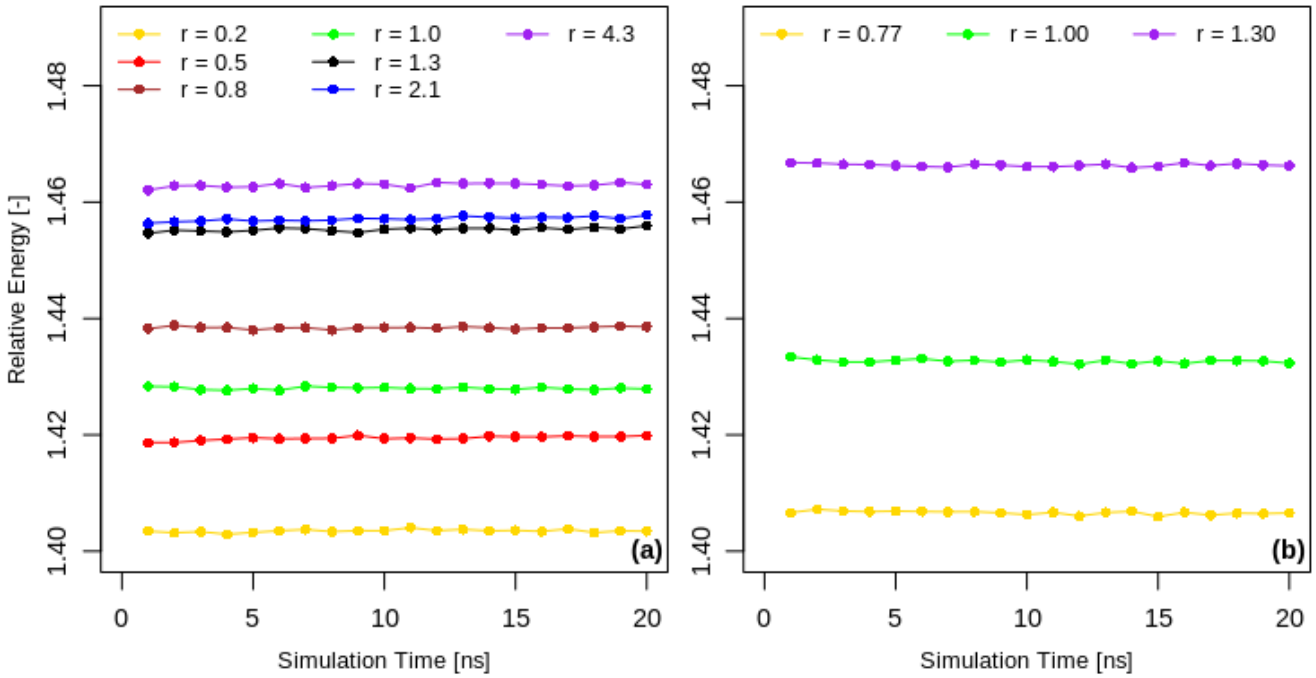

Figure S10: Shows the evolution of the systems' relative thermodynamic stability according to Equation 3 in the main text, when starting with one large particle (a) and starting with fully solvated ions (b).

Note that the curves in Figure S10 contain only the enthalpic contribution to the overall free energy. That all curves are more or less constant in time means that the enthalpy is not changing in time. However, since we know that the particle size, in our simulations starting from fully solvated ions, continues to increase, the entropic term in the total free energy will change.

SXI --- Nanoparticle stoichiometry evolution (simulations that started with a cluster)

To further investigate the evolution of the MD systems that started with a cluster, we highlight here the evolution of the stoichiometry of the total particle, its outer layer (5.8 Å) and the solution (Figure S11).

The stoichiometric system does not shed many Ca^{2+} or CO_3^{2-} ions during the 20 ns of simulation time (Figure S11a). Within the first 2 ns, the particle shed the largest amount of ions, in order to achieve a stable particle (Figure S10). Thereafter the particle started to build in some ions again (i.e growth). However, we observed for the non-stoichiometric systems that excess ions were shed in much larger amounts during the first ns and continued to shed some more during the remainder of our simulation time. Noteworthy, is that the amount of CO_3^{2-} shed from the particle in the r_{aq} = 4.85 system, slowly increased over time, while the amount of Ca^{2+} shed in the r_{aq} = 0.21 system remained approximately the same. The starting configuration of the non-stoichiometric systems had some ions in solution surrounding the particle, to maintain electro-neutrality. For r_{aq} = 0.21, 4 Ca^{2+}-ions and 17 CO_3^{2-}-ions (thus, a stoichiometry in solution of 0.24) were initially in the solution surrounding the particle and *vice versa* for r_{aq} = 4.85 (a stoichiometry in solution of 4.25). Therefore, it was possible for the r_{aq} = 0.21 system, to take up some Ca^{2+} ions from the solution (Figure S11c).

Only the outer layer of the particle in our simulations was given a certain stoichiometry, while the inner particle was built with a Ca^{2+}:CO_3^{2-} of 1 and was assumed to have the most stable configuration. Therefore, we also investigated the changes occurring in the external layer of the particle (Figure S11b). Particles containing a non-stoichiometric external layer tend to shed all the ions in their respective external layer, before they could initiate their growth.

The stoichiometry of the solution surrounding the particle stayed fairly constant throughout the entire 20 ns and the conditions in terms of stoichiometry were maintained (Figure S11c). The variations in stoichiometry of the bulk solution for the stoichiometric system with every ns of simulation time is due to the fact that there are initially no ions present in solution (for convenience stated as 1 in Figure S11c; e.g. the limit of Ca^{2+} and CO_3^{2-} ions going both to zero is 1) and that the addition of one ion has a relatively large effect on the stoichiometry. For

the non-stoichiometric systems, the initial amount of ions in the bulk solution was much larger. The stoichiometry of the outer layer of the particles varied over time for the non-stoichiometric particles (Figure S11d). For r_{aq} = 4.85, atoms were shed for the first 6 ns of simulation time, in order to reach a more thermodynamically favourable particle (nearly stoichiometric), before growth by addition of ions occurred. For r_{aq} = 0.21, atoms were shed throughout the entire 20 ns of simulation time and, therefore, required more time to obtain more favourable conditions for subsequent growth.

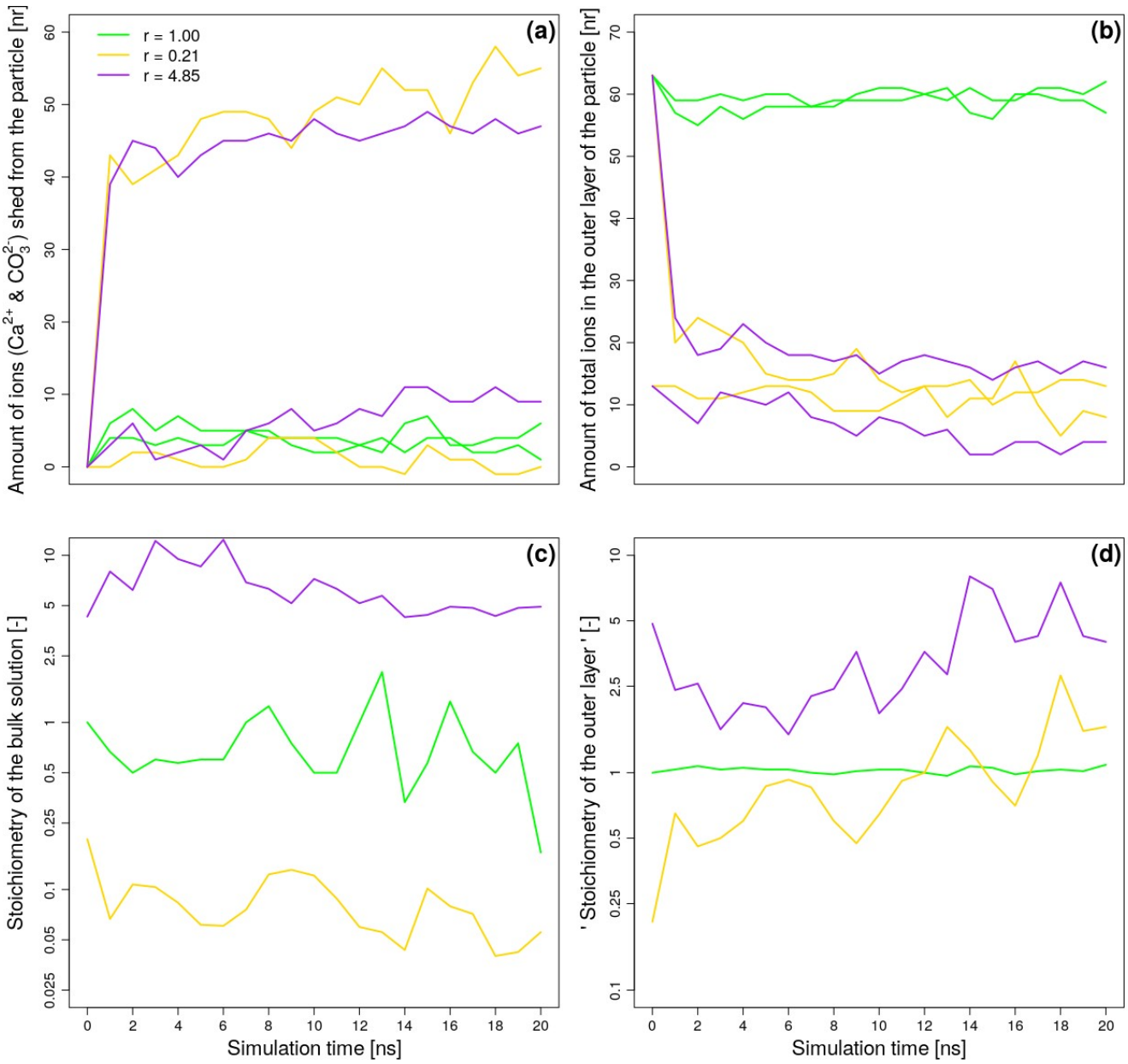

Figure S11: Illustrates the evolution of the particle created for the MD simulations with regards to the amount of ions it contained and the stoichiometry. Ca^{2+} and CO_3^{2-} atoms are shed from the particle (a), and are mostly shed from the predefined outer layer (b). As a consequence, the stoichiometry of the solution surrounding the particle is variable with time (c) and of the outer layer as well (d). In Figure a and b, the CO_3^{2-} (for r_{aq} = 0.21) and Ca^{2+} (for r_{aq} = 4.85) show the largest variation respectively.

SXII --- Stoichiometry evolution for simulations that started with fully solvated ions

Expectedly, the stoichiometry evolution for the stoichiometric system stayed fairly constant (r_{aq} = 1.42 after 20 ns of simulation time) and, thus, relatively stoichiometric throughout the entire simulation time. However, the systems that were initially non-stoichiometric became more extreme in their non-stoichiometry, while their relative stabilities remained more or less constant (Figure S10). The system with r_{aq} = 1.30, evolved to r_{aq} = 2.76 after 20 ns of simulation time and the system with r_{aq} = 0.77, evolved to r_{aq} = 0.37. Potentially, the difference in solution composition affected the systems differently.

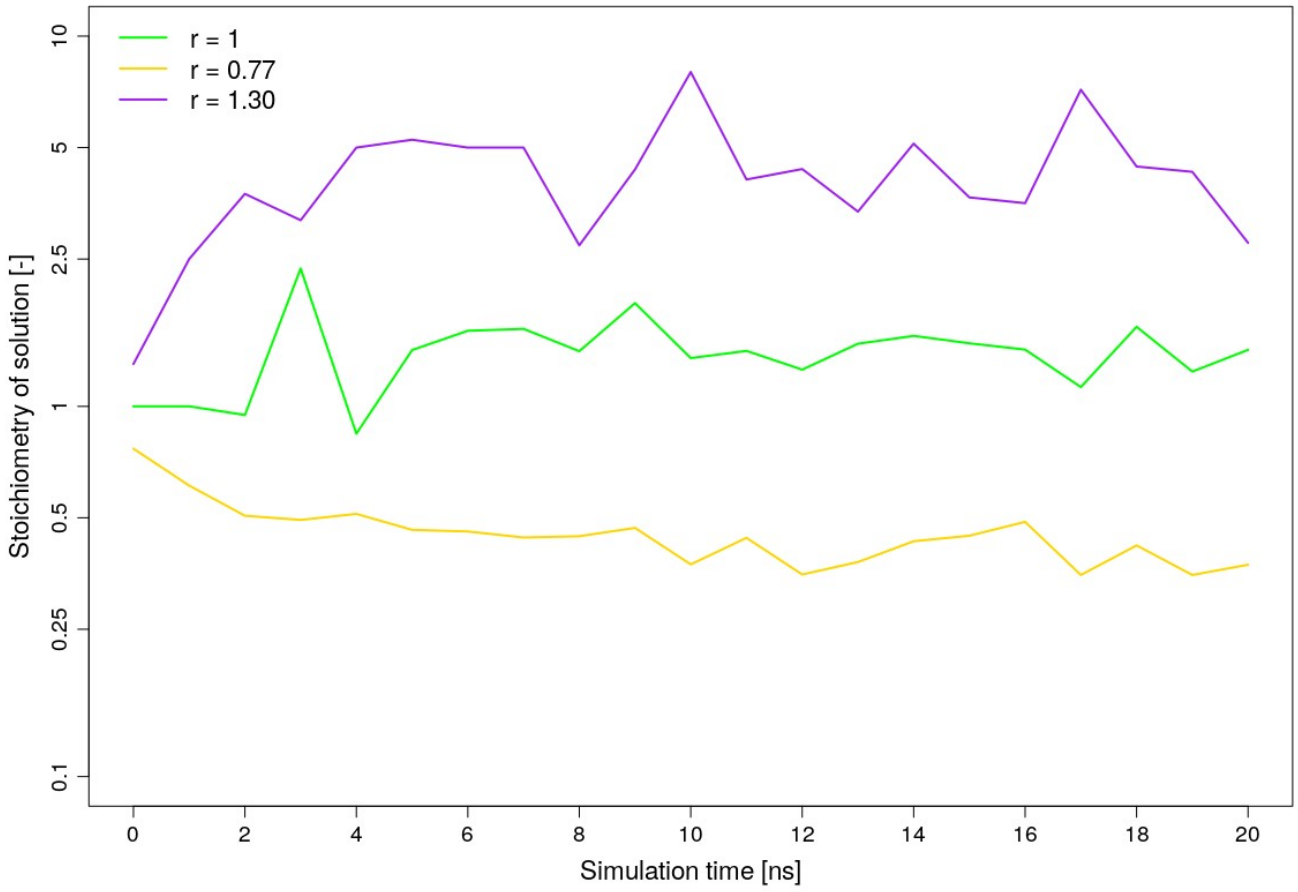

Figure S12: Stoichiometry evolution of the solution for the systems starting with fully solvated ions.

SXIII --- Ultra Pure Water (UPW) DLS measurements *versus* $CaCO_3$ DLS measurements

Pure water may show size distributions, because a difference in refractive index is defined for the measured system. However, such peaks for pure water only occur as a result of noise-on-noise. Typical count rates for a clean solution (i.e. pure water) are between 2 and 20 kcps,[20] but it depends also on the values for the absorption (in some specific cases such as gold particles) and the refractive index. Our measurements (for example the measurements of Figure 1) contained much larger count rates than 20 kcps. For the smallest Ω-value (= 70), we have derived count rates of 50 – 100 kcps. For the experiments conducted with Ω = 100, 150 and 200, we have count rates of 100 – 500 kcps. We have performed additional measurements of ultra pure water (UPW) (Figure S13.1) with the same values for absorption and refractive index as those for the $CaCO_3$ precipitation experiments.

The results below show both similarities and differences with the $CaCO_3$ precipitation experiments. The autocorrelation functions of UPW are roughly in the same range (correlation coefficient) as those of the $CaCO_3$ experiments (Figure S13.2). The fact that the physico-chemical conditions of the conducted $CaCO_3$ DLS experiments, related to Figure 1, is near or at the limit of what the Zetasizer Nano ZS can measure (lower limit in terms of concentrations), it is not surprising that they fall in the same range. However, the position of the peaks for the particle size intensity distribution of our experiments varies significantly from those of UPW. UPW shows invariably two peaks; one at the 1 – 10 nm size and another one at approximately 500 nm. This is in accordance with an ongoing debate about the formation of 'water clusters'.[21-27] Another typical feature of UPW is that the correlation function shows intermittent jumps and an overall flat line (Nobbmann, 2014), which is a result of noise-on-noise. This is in accordance of what we observed as well (topleft figure below).

The $CaCO_3$ DLS experiments show much less consistency in comparison with UPW water, with regards to the size range at which these intensity distribution peaks occur. For example, at every time step in Ω_{cal} = 70, intensity peaks within the 1 – 10 nm range are observed, but the intensity peaks at the larger size range are not invariable at all (Figure 1a). At Ω_{cal} = 100, the particle size intensity distribution peaks for the 1 – 10 nm range are absent

for each time step (Figure 1b). Only for Ω_{cal} = 200, the position of the particle size intensity distribution peaks coincide with those of UPW (Figure 1d *versus* Figure S13.1), but the intensity itself is quite large (> 15 %) if we compare them to the ones we observed for UPW (< 10 %).

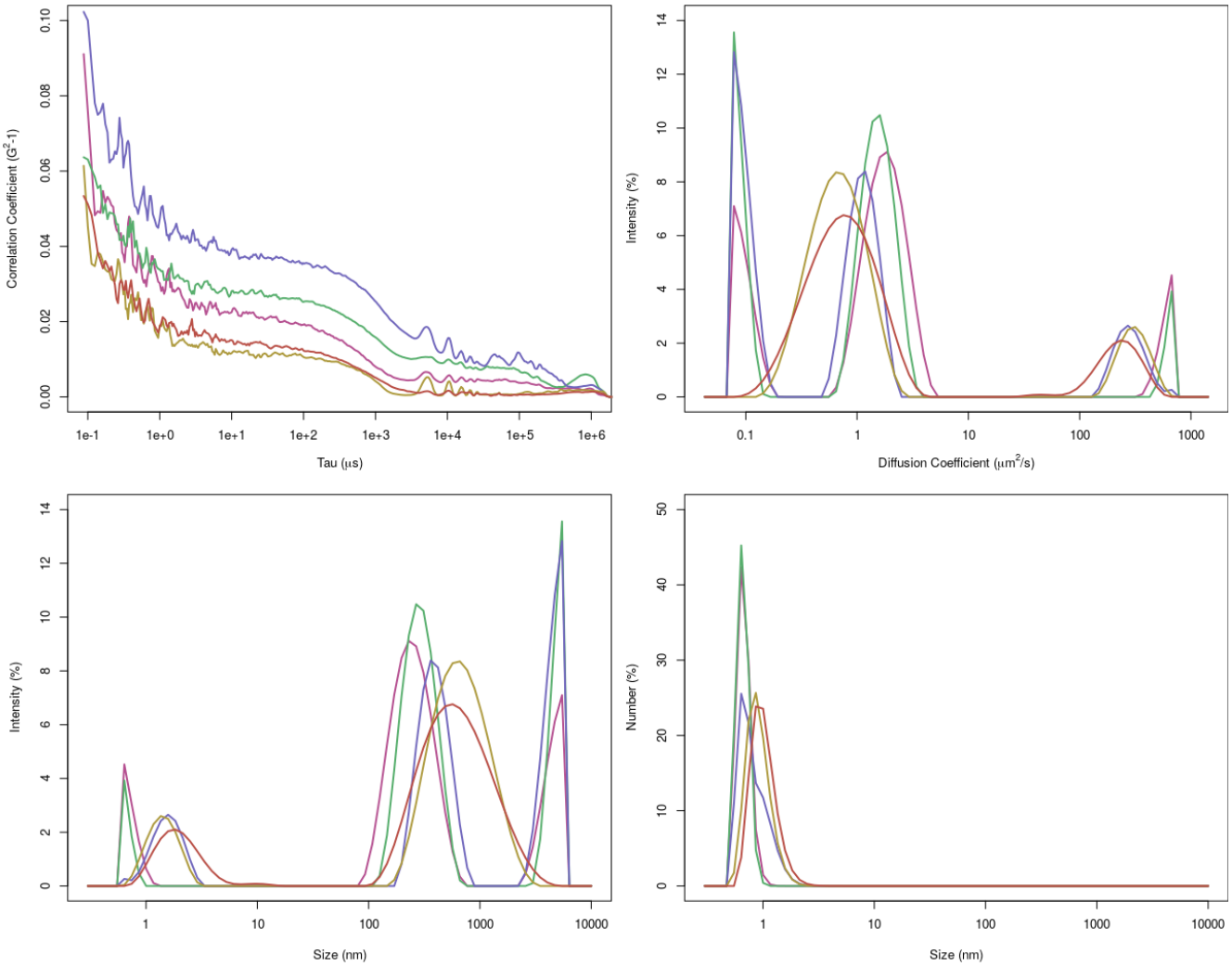

Figure S13.1: Illustrates 5 repeat measurements of UPW, which are defined by color. The RI for the measured material in the dispersant (water) was set at 1.55 (i.e. the same value as calcite). Topleft: Autocorrelation functions. Topright: Diffusion coefficient intensity distribution. Bottomleft: Particle size intensity distribution. Bottomright: Particle size number distribution.

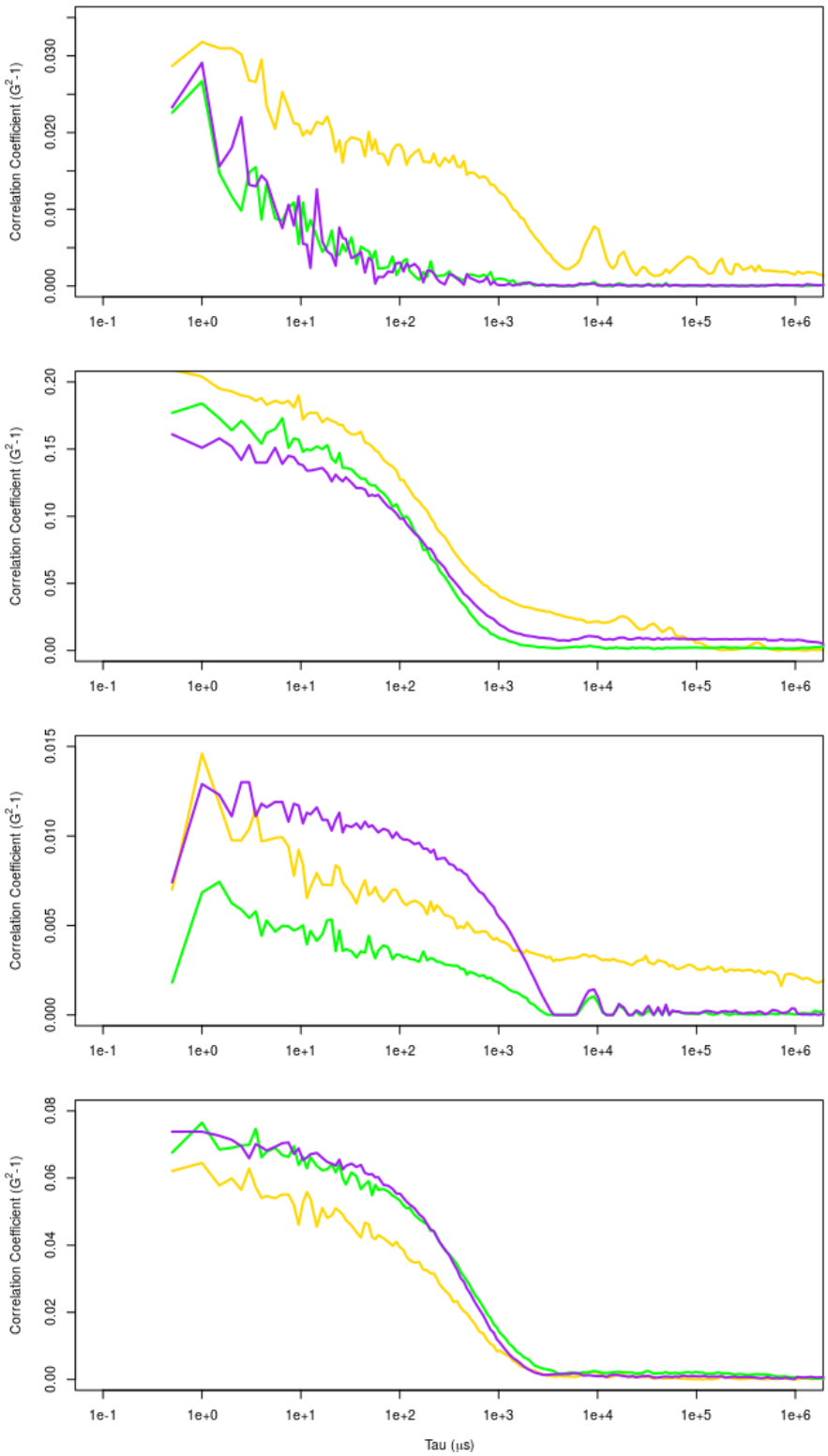

Figure S13.2: Illustrates the autocorrelation functions for the same measurements as those presented in Figure 1 in the submitted manuscript. The initial Ω_{cal} increases from top to bottom; 70, 100, 150, 200.

References

[1] Abramowitz, M.; Davidson, M. W. Diffraction of Light, 2012. Microscope Research Centre, Olympus.

[2] Abramowitz, M.; Davidson, M. W. Optical Birefringence, 2012. Microscope Research Centre, Olympus.

[3] Putnis, A. *An introduction to mineral sciences*. Cambridge University Press: UK, 1992.

[4] Natrella, M. *E-handbook of statistical methods*. NIST/SEMATECH: US, 2010. DOI: 10.18434/M32189

[5] Nielsen, A. E. *Kinetics of precipitation (Vol. 350)*. Oxford Pergamon Press: UK, 1964.

[6] Wolthers, M.; Nehrke, G.; Gustafsson, J. P.; Van Cappellen, P. Calcite growth kinetics: Modeling the effect of solution stoichiometry. *Geochimica et Cosmochimica Acta* **2012**, *77*, 121-134. DOI: 10.1016/j.gca.2011.11.003

[7] Zuddas, P.; Mucci, A. Kinetics of calcite precipitation from seawater: II. The influence of the ionic strength. *Geochimica et Cosmochimica Acta* **1998**, *62*(5), 757-766. DOI: 10.1016/S0016-7037(98)00026-X

[8] Team, R. (2015). RStudio: integrated development for R. RStudio, Inc., Boston, MA URL http://www.rstudio.com.

[9] Cho, S. Y.; Yetter, R. A.; Dryer, F. L. A computer model for one-dimensional mass and energy transport in and around chemically reacting particles, including complex gas-phase chemistry, multicomponent molecular diffusion, surface evaporation, and heterogeneous reaction. *Journal of Computational Physics* **1992**, *102*(1), 160-179. DOI: 10.1016/S0021-9991(05)80013-0

[10] Perini, F.; Galligani, E.; Reitz, R. D. An analytical Jacobian approach to sparse reaction kinetics for computationally efficient combustion modeling with large reaction mechanisms. *Energy & Fuels* **2012**, *26*(8), 4804-4822. DOI: 10.1021/ef300747n

[11] Dijkmans, T.; Schietekat, C. M.; Van Geem, K. M.; Marin, G. B. GPU based simulation of reactive mixtures with detailed chemistry in combination with tabulation and an analytical Jacobian. *Computers & Chemical Engineering* **2014**, *71*, 521-531. DOI: 10.1016/j.compchemeng.2014.09.016

[12] Dennis Jr, J. E.; Gay, D. M.; Walsh, R. E. An adaptive nonlinear least-squares algorithm. *ACM Transactions on Mathematical Software (TOMS)* **1981**, *7*(3), 348-368. DOI: 10.1145/355958.355965

[13] Bates, D. M.; Watts, D. G. *Nonlinear regression analysis and its applications (Vol. 2)*. Wiley: NY, 1988.

[14] Chambers, J. M. *Statistical Models in S*.; Wadsworth: Pacific Grove, California, 1992.

[15] Kashchiev, D. *Nucleation*; Elsevier: UK, 2000.

[16] Stumm, W. *Chemistry of the solid-water interface: processes at the mineral-water and particle-water interface in natural systems*; John Wiley & Son Inc.: NY, 1992.

[17] Declet, A.; Reyes, E.; Suárez, O. M. Calcium carbonate precipitation: A review of the carbonate crystallization process and application in bioinspired composites. *Reviews on Advanced Materials Science* **2016**, *44*(1), 87-107.

[18] Gomez-Morales, J., Torrent-Burgues, J., & Rodriguez-Clemente, R. Nucleation of calcium carbonate at different initial pH conditions. *Journal of crystal growth* **1996**, *169*(2), 331-338. DOI: 10.1016/S0022-0248(96)00381-8

[19] Garrels, R. M.; Christ, C. L. *Solutions, minerals, and equilibria*; Harper & Row: NY, 1965.

[20] Kirchhoff, B.; Rau, S.; Streb, C. Detecting and Preventing the Formation of Photosensitizer-Catalyst Colloids in Homogeneous Light-Driven Water Oxidation. *European Journal of Inorganic Chemistry* **2016**, *2016*(9), 1425-1429. DOI: 10.1002/ejic.201600065

[21] Maheshwary, S.; Patel, N.; Sathyamurthy, N. Structure and stability of water clusters $(H_2O)_n$, n = 8–20: An ab initio investigation. *Journal of Physical Chemistry A* **2001**, *105*(46), 10525–10537. DOI: 10.1021/jp013141b

[22] J. Kumar, F. Wang, G.R. Jenness, K.D. Jordan, A second generation distributed point polarizable water model, *Journal Chemistry Physical* **2010**, *132* (1), 14309–14312. DOI: 10.1063/1.3276460

[23] Furtado, J. P.; Rahalkar, A. P.; Shanker, S.; Bandyopadhyay, P.; Gadre, S. R. Facilitating minima search for large water clusters at the MP2 level via molecular tailoring. *Journal of Physical Chemistry Letters* **2012,** *3*(16), 2253–2258. DOI: 10.1021/jz300663u

[24] Li, F.; Liu, Y.; Wang, L.; Zhao J. Improved stability of water clusters $(H_2O)_{30–48}$: A Monte Carlo search coupled with DFT computations. *Theoretical Chemistry Accounts* **2012**, *131*(1163), 1–7. DOI: 10.1007/s00214-012-1163-5

[25] Hu, Q.; Lu, X.; Lu, W.; Chen, Y.; Liu, H. An extensive study on Raman spectra of water from 253 to 753 K at 30 MPa: A new insight into structure of water, *Journal of Molecular Spectroscopy* **2013**, *292,* 23–27. DOI: 10.1016/j.jms.2013.09.006

[26] Morawietz, T.; Behler, J. A density-functional theorybased neural network potential for water clusters including van der Waals corrections. *Journal of Physical Chemistry A* **2013**, *117*(32), 7356–7366. DOI: 10.1021/jp401225b

[27] Shu, L.; Obagbemi, I. J.; Jegatheesan, V.; Liyanaarachchi, S.; Baskaran, K. Effect of multiple cations in the feed solution on the performance of forward osmosis. *Desalination and Water Treatment* **2015**, *54*(4-5), 845-852. DOI: 10.1080/19443994.2014.908418

[28] Nobbmann, U. Tips & Tricks for Nanoparticle Characterization, 2014. URL materials-talks.com/blog/2014/11/17/tips-tricks-for-nanoparticle-characterization/